Multilayered liquid chemistries for active building facades

Raphael Kay[a,b,c], J. Alstan Jakubiec[c,d], Charlie Katrycz[a], Benjamin D. Hatton[a]

[a]Department of Materials Science and Engineering, University of Toronto
[b]Department of Mechanical and Industrial Engineering, University of Toronto
[c]John H. Daniels Faculty of Architecture, Landscape, and Design, University of Toronto
[d]School of the Environment, University of Toronto

Buildings designed with static[1] or minimally-programmable[2-5] surface properties cannot efficiently regulate solar flux, critically limiting operational energy performance[1,6]. The development of adaptive, building-scale materials, capable of achieving independent functional responses to their dynamic environment, has emerged as an important scientific challenge[7] that, if met, holds the potential to meaningfully reduce energy usage and carbon emissions at a global level[8-11]. Drawing from biological organisms that can tune the optical properties of their skin using multiple independent layers[12,13], we report a multilayered millifluidic interface for achieving independent and multifunctional material responses in buildings. We digitally inject and switch liquid-phase materials within confined milli-channel architectures, demonstrating independent and additive control over colour, scattering, and visible and infrared light transmission. This combinatorial optical tunability enables improved indoor visual and thermal comfort, increased light penetration, reduced overlighting, spectrally-decoupled visible and infrared light transmission, and annual modelled energy reductions of more than 43% over the best-performing comparable technology. With this fluidic mechanism established, new liquid chemistries can be engineered and readily integrated towards achieving net-zero energy consumption in buildings.

Buildings are the largest energy sinks on the planet, consuming almost three quarters of the U.S. national electricity supply[10], and approximately one third of the global energy supply[11]. Underpinning this energy footprint are operational inefficiencies arising from the inadequate regulation of solar ingress at the building facade[1,6,14].

Fundamentally, building facades represent the interface between the indoor and outdoor environments, responsible for regulating (i) the transmission of visible light (to illuminate the building interior), (ii) the scattering of light (to provide even daylighting across a space), and (iii) the transmission of infrared light (to maintain a comfortable indoor thermal condition). Convectional building facades and shading mechanisms, however, are either static or minimally-controllable, unable to perform these three optical functions (visible light transmittance, light scattering, and infrared light transmittance) dynamically, and certainly not independently, to achieve optimized, functional responses (e.g., transmitting light without heat)[1,6,14,15]. Mechanical blinds, shades, and electrochromic windows, for instance, cannot actively regulate daylight penetration (visible light transmittance) independent of infrared heat gain (infrared light transmittance), nor manipulate its spatial distribution within a room (light scattering)[1,6,14,15]. This restricted optical tunability is common to nearly every building facade on earth, and leads to large energy inefficiencies and undesirable variations in interior illuminance and temperature, drastically increasing the energy required to heat, cool, and light the indoor space[1,6,14,15].

To meaningfully limit this operational energy consumption[16], building facades would greatly benefit from decoupled switchable control over visible light transmittance, light scattering, and infrared light transmittance. Developing materials that can achieve dynamic and independent programmability over total transmission, scattering, and spectrally-selective absorption is accordingly among the most pertinent unmet challenges in building design[8,9] that nearly all existing and proposed mechanically[1,17-22], electrically[2-4,6,23-27], optically [5,6,24,28-30], hygroscopically[31,32], and thermally-actuatable[5,6,28-30,33,34] chromogenic systems remain unable to address.

In contrast, a select number of biological organisms have evolved a multilayer surficial architecture to adaptively tune independent optical properties at their interface. In certain species of squid, for example, active camouflage is achieved through the independent and cooperative action of multiple individually-addressable

layers within the skin[13,35] (Fig. 1b). Under neural direction, squid simultaneously control both a pigmentary layer of chromatophore organs and a structural layer of protein cells (iridophores)[12,36,37], mediating surface colour, spectral reflectance, and spatial patterning by coordinating the expansion and contraction of the upper layer of pigmentary sacs[35] and the active reconfiguration of nanostructural iridophores below[13,35,38-40]. Large shifts in spectral reflection peaks occur along surface regions where both pigmentary and structural layers are overlaid (Extended Data Fig. 3c-j), enabling combinatorial, and perhaps even additive, optical responses. The panther chameleon has also evolved a multilayered infrastructure within its skin, leveraging a two-tiered system of photonic crystals, each with an independent morphology and function[41] (Fig. 1a). Colour change is regulated through the uppermost photonic layer, as chameleons actively manipulate the periodicity of guanine nanocrystals to selectively disrupt and reflect light. Thermoregulation, on the other hand, is achieved through the lowermost photonic layer, where populations of regularly-arranged iridophore cells strongly reflect radiation in the near-infrared region.

Independently-tunable and -functional multilayer interfaces enable combinatorial physiological responses in organisms. We hypothesize that, by developing building-scale analogues for these biological systems, we can achieve similarly-sophisticated optical behaviours (Extended Data Fig. 3). Here, drawing from the multilayer and multifunctional optoregulatory mechanisms in biological organisms, we report a multilayered and multifunctional interface for accomplishing independently-tunable light transmission, light scattering, and spectrally-selective light absorption in buildings (Fig. 1c). We borrow microfluidic principles from biology[42-46] to develop a large-area millifluidic multilayer, and demonstrate additive, functionally-independent, and multifunctional optical responses through the digital injection and switching of confined fluids therein (Fig. 1d-e). Compared to conventionally-limited solid-phase chromogenic technologies, we show how small volumes of fluid can be chemically designed and easily manipulated over large surficial areas to achieve inexpensive, rapidly-switchable, and spectrally-tunable optical responses in building-scale materials. Finally, in simulation, we demonstrate that independent digital control over three sequential fluid layers along a building – to regulate optimal degrees of visible transmission, visible scattering, and infrared transmission – can accomplish savings of 75% on heating energy, 20% on electric lighting energy, and 43% on total operational energy, compared to the best available electrochromic technology. These results suggest a new fluidic paradigm for buildings, where fluid layers within a facade can behave in concert, and individually, as chemically- and functionally-programmable optical filters. Such a general fluidic infrastructure could radically impact the way we design buildings.

Results

Functional fluidic optical controls

We fabricated bi- and trilayer optically-transparent millifluidic devices (15x15x2 cm^3). Fluid layers were machined from rigid PMMA plates (0.3 cm thick), and were adhered using common vapour-polishing protocols[47] (Extended Data Fig. 1). PMMA multilayers were designed with stacked parallel-channel architectures. The ends of each channel structure (1.5 mm deep) were connected to small independent liquid reservoirs (14 mL) and, using digitally-controlled syringe pumps, we toggled between optical states for each fluid layer through the controlled switching of liquids therein. Channels became largely imperceptible when filled with a liquid (mineral oil) of an equivalent refractive index to PMMA (~1.48) (Extended Data Fig. 2).

Distinct building layers should correspond to independent optical functions, and a quad-layer interface was conceptualized to enable individual control over the injection of (i) a selectively-absorbing coloured fluid, (ii) a visible- and infrared-absorbing shading fluid, (iii) a light-scattering diffuser fluid, and (iv) an infrared-absorbing (but visibly-transmitting) thermoregulatory fluid (Fig. 1b). Functional and energetic benefits were demonstrated individually for each layer, and combinatorially for various multilayer states.

Additive multilayered spectrally-selective absorption. To demonstrate the working principle of multilayer fluid injection within our device, we injected several visible dyed solutions within a bilayer millifluidic interface (Fig. 2a-b). We exemplified additive optical control by sequentially activating two distinct spectrally-selective fluid layers: a spectrally-selective blue coloured fluid, and a spectrally-selective yellow coloured fluid (Fig. 3c, i-iv). When

overlapping, these fluid layers behaved as additive spectrally-selective filters, transmitting light with a distinct green colour. Quantitatively, we verified well-established colour theory by showing that when two fluid-layer 'filters' are added in series, the transmission spectra through the combined fluid bilayer is equal to the product of the transmission spectra of each layer independently (Fig. 3c, vi). This additive colour-filtering mechanism therefore allows us to design additive optical responses: for instance, we demonstrated additive colour + dimming by activating both a switchable colour layer and switchable absorbing layer in series within a bilayer interface (Extended Data Fig. 4, Supplementary Video 1). We characterized optical transmission for colour layers when activated individually, and then when activated simultaneously with a dimming (absorbing) phase, illustrating the possibility for a coordinated multifunctional response.

These results not only demonstrate independent, multilayered fluid control generally, but also show the ease with which the chemistry of a fluid can be tuned to achieve spectrally-selective light absorption (whether in the visible range as shown here, or in the infrared range as shown later). In particular, control over spectrally-selective absorption in the visible range at the surface of a building could enable dynamic control over interior colour. Tunable visible spectral absorption (colour change) could have important implications for biological circadian dynamics[48-50]. It has been suggested that buildings that can modulate interior colour could improve occupant alertness, and overall human comfort and health[48-50].

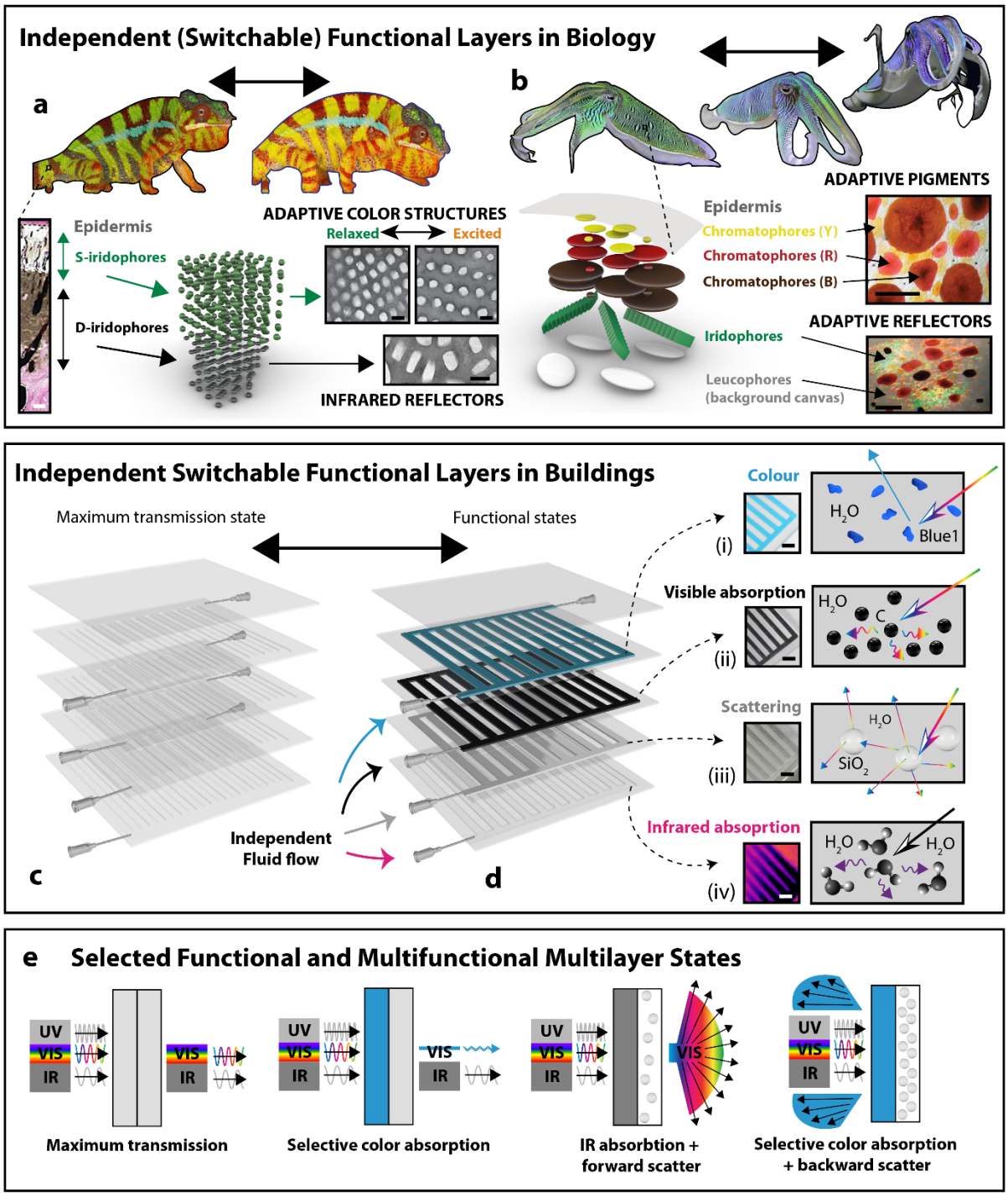

Figure 1. Biological inspiration for fluidic multilayer. (a) Colour change in the panther chameleon, achieved using a multilayer architecture of active photonic crystals. **(b)** Colour change in the cuttlefish, achieved using coordinated actuations within a multilayer of pigmentary and structural elements. **(c-d)** Schematic for achieving independent multilayered switchable responses in building facades, where switchable fluid flow within distinct layers can enable multiple distinct optical functions. **(e)** Schematic exemplifying several functional or multifunctional states, achieved through coordinated fluid injections within a bilayer. The fluid multilayer acts as an additive light filter for incoming light. Scale bars: (a) white, 20 µm; black, 200 nm; (b) 1 mm; (d) 1 cm. Images in (a) reproduced from [41], published under a Creative Commons license (http://creativecommons.org/licenses/by/4.0/). Images in (b) reproduced under license from [13], and from [51].

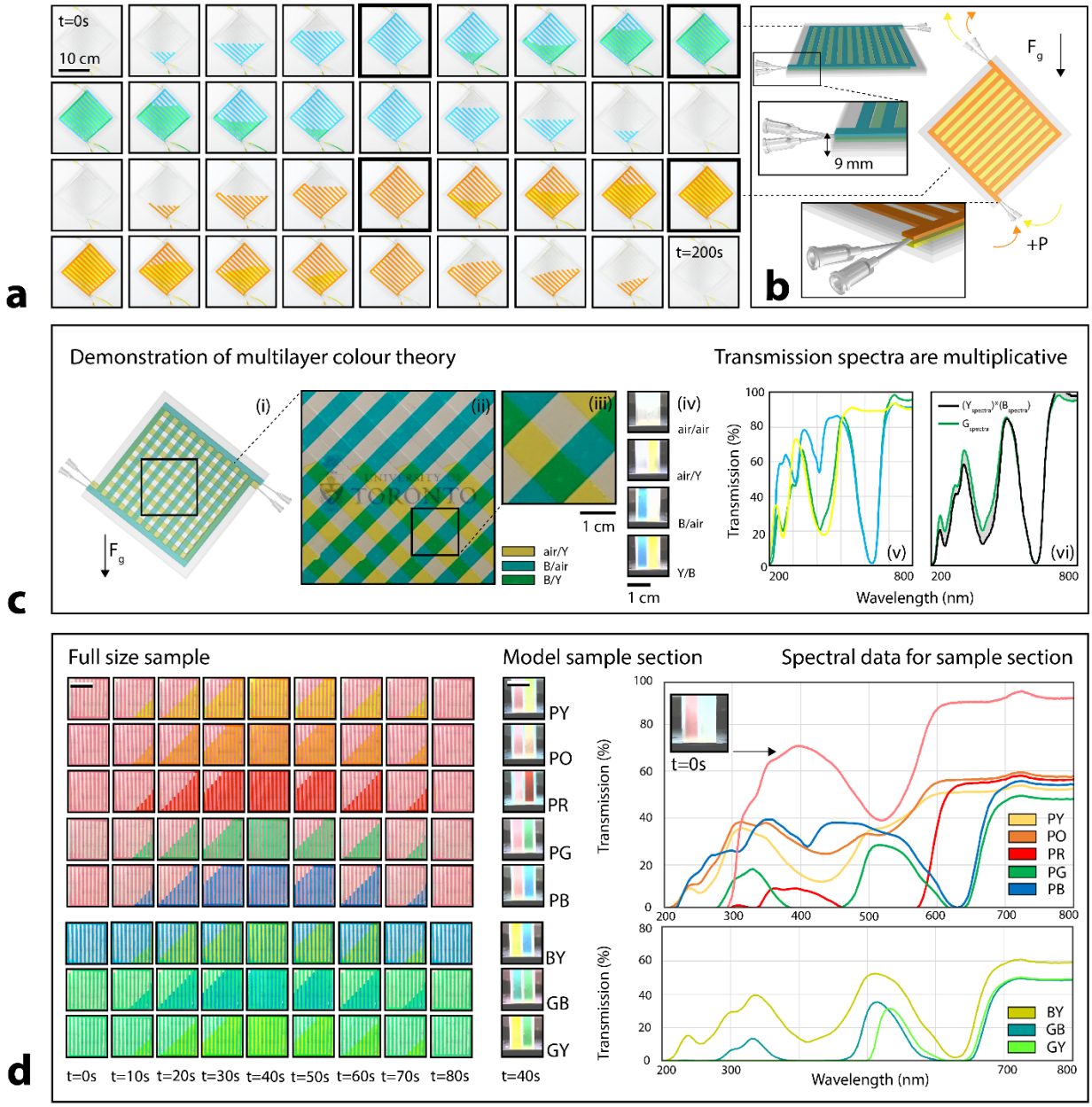

Figure 2. Demonstration of working principle of additive fluidic multilayer absorption. (a) Still frames across two complete cycles of fluid injection and retraction, demonstrating four unique coloured states (bolded frames) within fluidic devices. **(b)** Design of bilayer device. **(c)** Overlapping crosshatch bilayer design, demonstrating periodic instances of additive colour filtering, as well as instances of single-layer colour filtering. Spectral measurements (v) were taken using 'model' bilayer sample section, shown in (iv), and illustrate transmission spectra from both independent layers (yellow, blue) and combined bilayer (yellow and blue). We confirm that transmission spectra are multiplicative, where B/Y bilayer spectra (green curve in (vi)) are equivalent to multiplication of B spectra and Y spectra (black curve in (vi)). **(d)** Additive multilayered absorption (demonstrated through colour change), achieved through various combinations of overlapping dyed aqueous fluid pairs. Left scale bar is 10 cm. Right scale bar is 1 cm. Spectral measurements were taken using modelled sample sections (middle of panel). Images of device were rotated 45°. In experiments, multilayer devices were filled on a 45° angle to limit horizontal channels and air bubble formation.

Active solar transmission and switchable shading. The ability to actively modulate the transmission of solar radiation for control over interior light intensity is a crucial function for a high-performance building. If large-area switchable shading could be consistently achieved, models suggest that annual operational energy consumption of buildings could be reduced by up to 50%[9,52]. In our recent work, we demonstrated that reversible fluid injections could be leveraged within confined fluidic windows to spatiotemporally control total light transmission by over 90% in indoor environments[53]. To dynamically control interior light transmission here, we injected aqueous suspensions of paracrystalline carbon (carbon black) within a bilayer millifluidic interface (Fig. 3a-c, Supplementary Video 2). We embedded the fluid interface within a scaled-down 'shoebox' physical room model (30x30x15 cm^3) fit with an interior light sensor (setup in Extended Data Fig. 5). This physical model allowed us to characterize transmitted visible light across a multilayer injection sequence for various suspension concentrations. Importantly, we demonstrated maximum reductions in interior light intensity of 100% when the layers were completely filled with aqueous suspensions of a minimum particle concentration of 2 mg/mL (Fig. 3d). Light transmission within the visible spectrum was spectrally-uniform, and, as expected, intensity decreased with particle concentration of shading fluids (Fig. 3e).

The Beer-Lambert law, shown as equation (1), postulates that absorbance within each fluid layer should be equal to the log of the ratio of incident I_0 to transmitted I light power through that layer, and is given by the product of the molar absorptivity ε, the layer thickness b, and the particle concentration c. As expected, absorptive shading in our layers was demonstrated to follow Beer-Lambert[54], and we showed reductions in transmitted light intensity in agreement with equation (1) when we activated a second shading fluid layer behind the first, effectively doubling b (Fig. 3f, dotted red curve). We note this method is also mathematically identical to squaring the transmission spectra for a single fluid layer at every wavelength, and provides an estimated spectra within a few percent of our measured values.

$$(1) \qquad \log_{10}\frac{I_0}{I} = \varepsilon bc$$

We used these measured transmission spectra to simulate the optical properties of fluid layers in buildings. Transmission spectra corresponding to differently concentrated suspensions of shading particles were used to describe glazing materials in simulation. We leveraged a well-established and widely used backwards light-ray-tracing simulator and renderer (Radiance)[55] to model diffuse and specular daylight penetration and compare illuminance across a standard digitally-modelled space while clad in switchable fluid layers. Luminance, compared across three different concentrations of shading particles (Fig. 3g), was rendered with six ambient bounces, using weather data from Toronto, Canada, within a conventional two-zone office, 9.0 m wide (N-S direction) and 12.7 m deep (E-W direction), with glazing on the south and west faces (window-to-wall ratio of 68 and 57%, respectively). Daylight availability was simulated (Fig. 3h) within a smaller one-zone reference office (described in[56]), 3.6 m wide (E-W direction) and 8.2 m deep (N-S direction), with a south-facing window (window-to-wall ratio of 40%).

In simulation, we demonstrated how light transmission and light penetration depth could be decreased by increasing particle concentration, exemplified using layers with five different concentrations of shading particles in the middle of a November day (Fig. 3h). Annually, as expected, the fraction of interior space conventionally defined as underlit (< 100 lux) and supplementarily-lit (100 - 300 lux) increased with concentration, while the fraction of space acceptably-lit (300 - 3000 lux) and excessively-lit (> 3000 lux) decreased with concentration (Fig. 3i-l).

Switchable fluids provide us with a vehicle to modulate both the penetration depth of visible light and the interior light intensity within an indoor space. Because interior solar heat gain, described by a SHGC (equal to the fraction of solar radiation admitted through a window at a fixed incident solar radiation spectra), is largely dependent on optical transmission, the performance implications of switchable fluid absorption are significant. To demonstrate the associated improvements to building energy efficiency, we used a well-established computational building energy and thermal modelling tool (EnergyPlus) to estimate the annual energy required for heating and cooling a standard space in Toronto, Canada (the same one-zone office as described above). We compared heating

and cooling for maintaining a constant indoor temperature within the space when clad with (i) a low-emissivity 'control' window (SHGC = 0.71; $T_{visible}$ = 0.81; U-value = 1.81 W/m^{2}K), and when additionally clad with (ii) our fluid interface that can modulate between a transmitting state (empty air channels) and absorbing state (2 mg carbon/mL water). Within EnergyPlus, heating and cooling loads were calculated using the conduction finite difference solution algorithm[57,58] with hourly historical environmental data on outdoor temperature, cloud cover, solar intensity (direct and diffuse radiation) and solar elevation, and accounted for thermal properties (e.g., conductivity, emissivity, heat capacity) of indoor materials. For simplicity, we assumed no internal heating loads from lighting, occupants, or equipment (additional zone details, temperature setpoints, and material properties described in Methods). For the energy simulation, we developed a simple control algorithm to instantaneously 'inject' the absorbing fluid at hourly timesteps when the interior space needed to be cooled (i.e., when indoor temperature > setpoint temperature). The shading fluid absorbs light in both the visible and infrared spectrum that would otherwise be converted to excess heat indoors. We modelled this fluid layer on the outside of the control window, minimizing conductive heat gain following solar absorption. In simulation, the infrared-absorbing layer was activated during peak solar loading during the day in both winter and summer seasons (operation of layer for sample day in November demonstrated in Extended Data Fig. 6a), dramatically decreasing the window solar heat gain and total indoor operational energy requirement (Extended Data Fig. 6b-c). Annually, we showed that switchable control of a shading fluid could reduce the operational energy requirement for indoor space heating and cooling by 51%, exceeding the most ambitious estimates for building energy savings with existing adaptive shading technologies[9,52].

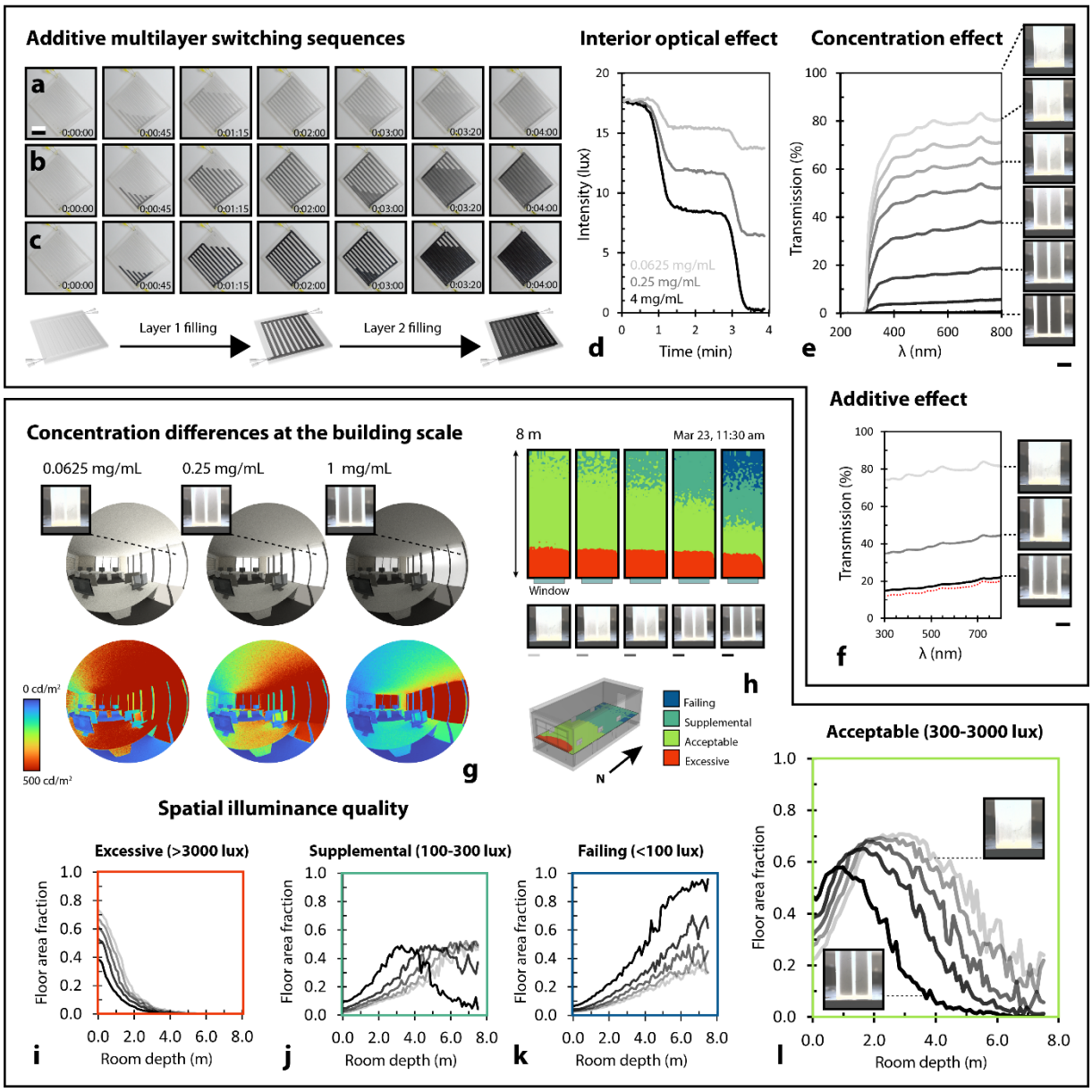

Figure 3. Active fluidic multilayer shading. (a) Still frames across three independent injection sequences within bilayer, for three fluids of different particle concentrations (concentrations in d). Scale bar is 5 cm. **(d)** Corresponding interior light intensity measurement within model room (experiment demonstrated in Extended Data Fig. 5). **(e)** Measured transmission spectra (within cuvette) as function of particle concentration. Curves correspond to transmission spectra of fluids concentrated at 0, 0.0625, 0.125, 0.25, 0.5, 1, 2, 4 mg C/mL H_2O, from top to bottom. **(f)** Measured transmission spectra (within cuvette) as function of number of activated layers. Images show cross-section of bilayer cuvette. Fluid concentrated at 1 mg C/mL H_2O. Top curve represents spectra of empty cuvette. Dotted red line shows Beer-Lambert model estimate for completely-filled bilayer, calculated by doubling optical path length of spectra for half-filled bilayer in equation (1). **(g)** Backward ray-tracing renders illustrating daylighting differences for differently concentrated fluid window layers. **(h)** Daylight availability simulations demonstrating differences in available daylight across a modelled interior space for differently concentrated fluid window layers. Window optical properties derived from transmission properties of fluids concentrated at 0, 0.0625, 0.125, 0.5, 1 mg C/mL H_2O, from left to right. Failing, supplemental, acceptable, and excessive daylighting are defined, respectively, as <100 lux, 100-300 lux, 300-3000 lux, and >3000 lux. **(i-l)** Floor area fractional spatial illuminance quality for differently concentrated fluid layers as a function of depth within the space. Illuminance values are taken as central (width) value at each depth within the space. Scale bars in e, f, h are 5 mm.

Active directionally-tunable light scattering. The ability to modulate light transmission can be augmented by the ability to cooperatively modulate the *distribution* of light transmission (i.e., to spread the same number of photons over a larger area). In buildings, light scattering can reduce excessively-lit areas, increase the depth of daylight penetration, and improve total illumination – with significant implications for human health and productivity[59,60]. Silicon oxide particles with nanoscopic topographical features scatter incident light. To demonstrate directional control over light scattering using fluids at a macroscopic scale, we injected aqueous suspensions of monodispersed silica microspheres (Fig. 4a) and standard silica particles (Fig. 4b-g) at various concentrations within a bilayer millifluidic interface (Fig. 4b). We focused an incident light beam (14 klm normal to the surface) on multilayered interfaces filled with silica fluid suspensions of varied concentrations, and demonstrated that the direction of light scattering could be tuned with concentration (Fig. 4b-c). Higher silica concentrations corresponded to substantial back-scattering (like a Lambertian reflector) (Fig. 4c, bottom), while lower silica concentrations corresponded to forward-scattering (like a forward diffuser) (Fig. 4c, top). Visible light transmission decreased with particle concentration as predicted (Fig. 4d), however the fraction of transmitted light scattered, as opposed to directly transmitted, increased with particle concentration (Fig. 4e). This represents a functional limit to this mechanism: as light transmission increases (inversely with particle concentration), the ability to scatter light decreases (Fig. 4f-g).

Given an identified functional range of fluidic light-scattering control, we used ClimateStudio to compare luminance across an indoor space (same two-zone office as before) when clad in a regular window and in a fluid layer with a population of scattering particles (4 mg SiO_2/mL H_2O, visible transmission spectra in Fig. 4d) (Fig. 4h-i). We controlled for total light transmission, comparing interior light distribution using both a standard window and fluid layer with a visible light transmissivity (T_{vis}) of 40%. We calculated daylight availability (same one-zone reference office as before), and found that the fluid scattering layer, able to scatter 95% of incident light, enables both reduced overlighting (defined as > 3000 lux) in the winter months (with a low solar azimuth) (Fig. 4j), and increased light penetration depth in the summer months (with a high solar azimuth), when compared to the control window (Fig. 4k). Light diffusion enables annual improvements to optical occupant comfort by increasing daylight autonomy (> 300 lux) (Fig. 4m) and decreasing the fraction of underlit floor space (< 300 lux) (Fig. 4n-o), without compromising excessive daylighting (Fig. 4l)[61]. With optical scattering, more daylight is distributed to reflective interior surfaces, and less daylight is absorbed by (lost to) the floor. This increase in useable daylight greatly reduces the need for supplemental electrical lighting deep within the space (when illuminance is below 300 lux), leading to annual electric light energy savings of 18%, and 9% within room depths of 3-6 and 6-9 m, respectively (Fig. 4p), for a total electric lighting load reduction of approximately 10% (Fig. 4q). Annually, this calculated reduction in electric lighting also reduces the unwanted spatial heat gain by 101 kWh. We found that over half of this heat is supplied to the space when unfavourable (i.e., when the room is attempting to cool the space), further increasing the workload and energy composition of the cooling system.

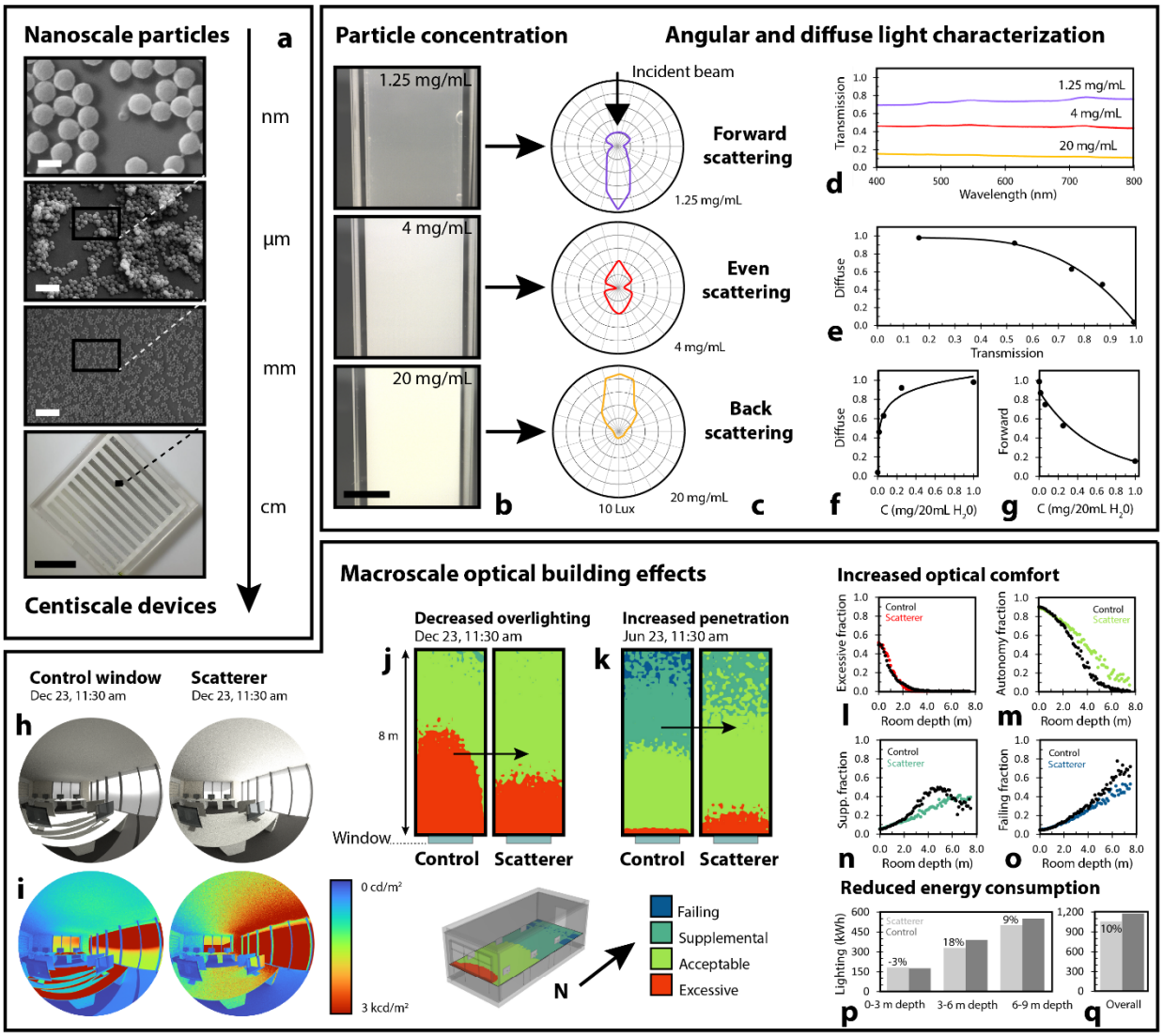

Figure 4. Active fluidic directionally-tunable light scattering. (a) SEM and photographic images illustrating multiscale fluidic mechanism, utilizing nanoscale particle features for macroscale optical control. Scale bars, from top to bottom, are 4 µm, 2 µm, 250 nm, and 5 cm. **(b)** Images of three cuvettes, each filled with an aqueous suspension of scattering particles. Scale bar is 5 mm. **(c)** Differentially-scattered light profiles for each fluid concentration in (b). Increasing concentrations correspond to increasing back scattering. **(d)** Suspensions with higher particle concentrations transmit less visible light. **(e-g)** Suspensions with higher particle concentrations scatter more visible light (f). Therefore, as transmission increases, relative scattered (diffuse) lighting decreases (e). **(h-i)** Backward ray-tracing renders illustrating spatial daylighting differences between regular control window and window with scattering particles. The scattering window enables visibly-deeper light penetration. **(j)** Daylight availability simulation demonstrating the degree to which a scattering layer can reduce excessive illuminance. **(k)** Daylight availability simulation demonstrating the degree to which a scattering layer can improve daylight penetration. **(l-o)** Scattering layers improve optical comfort, having a small effect on excessive illuminance throughout the year (l), but decreasing the fraction of indoor space that requires supplemental electric lighting (n-o), and increasing the fraction of indoor space that requires no electric lighting (m). **(p-q)** As a result, the scattering layer enables reductions to electric lighting usage at depths between 3-9 m, enabling 10% annual reductions in electric lighting energy consumption.

Active daylight-independent infrared modulation. Developing building interfaces capable of independently regulating visible and infrared light is sometimes considered the most important unmet challenge in building design[8]. Existing strategies to regulating the ingress and egress of infrared light include low-emissivity[62] and spectrally-selective[63] window coatings, which are both static and limited in variable climates[64]. In the heat of the summer, for instance, an ideal window should be transparent to visible light, but opaque to infrared light. Alternatively, in the cold of the winter, an ideal window should be transparent to both visible and infrared light[64].

Because the optical properties of fluids can be chemically-tuned, switchable fluid injection represents a promising mechanism to achieve switchable, spectrally-selective light absorption (i.e., control over infrared light separately from visible light). To modulate infrared light transmission largely independently of visible light transmission, we injected a series of liquids that are transparent in the visible spectrum but partially-absorbing in the infrared spectrum within a bilayer millifluidic interface (Fig. 5b). Liquids that absorb light in the infrared region can block unwanted solar heat from entering a building. When we replace an air layer with water, for instance, the transmitted visible radiation (350-750 nm) through the interface is reduced only mildly (ΔT_{vis} = 16%), however the transmitted infrared radiation (751-2500 nm) decreases considerably ($\Delta T_{infrared}$ = 76%). This is shown by the effective temperature measurement from an infrared camera in Fig. 5a.

To demonstrate the impact of this active fluid injection and infrared switchability on interior temperature, we developed a simple scaled-down room model (30x30x30 cm^3) clad on one side with our fluid layer (setup in Extended Data Fig. 7). We radiated the room from the outside using a 100-W incandescent light until a thermocouple measuring the temperature of a PMMA sheet indoors reached a thermal equilibrium of 39 °C (after 30 minutes). We then injected 14 mL of water (absorption properties in Fig. 5b) within the fluid layer, which absorbed a substantial portion of the incident infrared radiation. The water provided visibly-independent shade in the infrared region, and allowed the PMMA sheet to cool to 32 °C within fifteen minutes (the room was well-ventilated to account primarily for radiative thermal transfer).

To estimate the associated energy savings in buildings, we used EnergyPlus to compare the annual energy required to heat and cool a standard space (one-zone reference office) to a temperature setpoint (same as above) when clad with a low-emissivity 'control' window (SHGC = 0.71; T_{vis} = 0.81; U-value = 1.81 W/m^2K), and when additionally clad with a fluid layer that can modulate between an infrared-transmitting state (empty air channels) and infrared-absorbing state (0.015625 mg carbon/mL water). The average visible transmission of both these states is above 75% (transmission spectra in Fig. 5b). As before, we modelled our fluid layer on the outside of the control window, and we assumed no internal heating loads from lighting, occupants, or equipment (zone details, temperature setpoints, and material properties are described in Methods). In our model, the infrared-absorbing layer was primarily activated during peak solar loading during the day in both winter and summer seasons (operation of layer for sample day in November demonstrated in Fig. 5d), decreasing the unfavourable window solar heat transfer (Fig. 5e) and total operational energy requirement (Fig. 5f). Annually, we found that the multilayer with active infrared absorption reduced the internal heating and cooling loads by 25% when compared to the control window. This significant result represents the first quantitative demonstration of the potential for performance improvements to buildings using functional liquids with decoupled infrared and visible light transmission switchability.

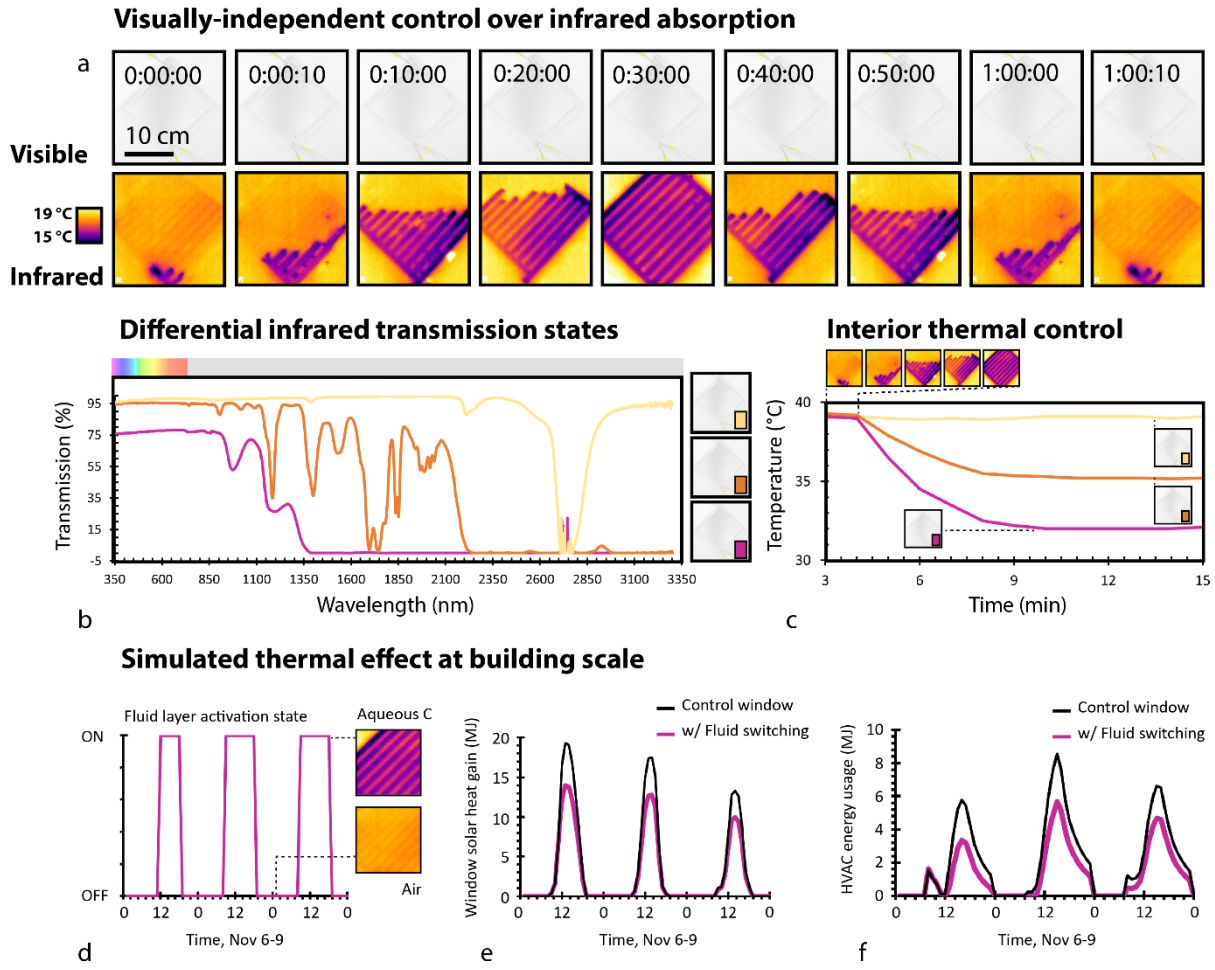

Figure 5. Active fluidic visibly-decoupled infrared-switchability. (a) Water injection and retraction sequence, imaged in the visible and infrared spectrum. While there are no noticeable changes to visible transmission, infrared transmission is decreased with water injection. Experiment conducted in the horizontal plane for ease. **(b)** Differential infrared transmission across three independent fluids (air, glycerol, and 0.015625 mg carbon/mL water, from top to bottom) that each have high transmission in the visible spectrum. **(c)** Temperature measured behind a fluid multilayer across an injection sequence of each fluid from (b). Air represents control injection. Experiment illustrated in Extended Data Fig. 7. **(d-f)** Simulated effect of infrared-switchability in buildings. Reference one-zone office for energy modelling illustrated in Fig. 6a. (d) Control schedule for activating infrared-absorbing layer within glazing. (e) Window solar heat gain and (f) associated energy usage over three-day period for both regular double-pane control window and for control window with additional switchable fluid layer. Differences in total energy predominantly reflect differences in cooling energy due to overheating.

Total energy use reduction through combinatorial multilayer optical tunability

While active control over visible (vis) light transmission, infrared (IR) light transmission, and visible light scattering (scattering) enables substantial improvements to building energy performance individually, control over these functional layers cooperatively enables advanced combinatorial responses, and among the most significant parameter spaces ever developed for optical control in architecture. Existing static building facades cannot actively control vis transmission, IR transmission, or scattering (Fig. 6c). All dynamic building facades and shading components, including manual and electric blinds, electrochromic (EC) windows, and roller shade (RS) devices can control vis-IR properties, but with no independence between properties (Fig. 6c). Our fluid multilayer is the first

device for a building interface capable of controlling vis-IR-scattering independently across multiple degrees of freedom, in our case maximally through three (Fig. 6c).

To estimate the performance potential of this material system, we used EnergyPlus to compare the annual energy required to heat, cool, and light our one-zone reference space when clad along the south facade (window-to-wall ratio of 88%) in (i) our fluid multilayer, (ii) a state-of-the-art EC window, (iii) a RS, and (iv) a static low-emissivity window. For consistency, we simulated the operation of all dynamic systems using the same control algorithm (Fig. 6b), in each case aiming to minimize total energy usage at hourly timesteps (combined heating, cooling, and electric lighting), while maintaining a minimum daylight threshold of 300 lux, and limiting overlighting (> 3000 lux) to 10% at any point across the space (details of iterative control algorithm in Methods). We modelled the EC window to switch between its four standard possible states, the RS between its two standard states (up and down), and our fluid multilayer to switch between all combinatorial possibilities of 16 total fluids across three distinct layers (all base state optical properties in Fig. 6b). To appropriately account for building integration, the RS was modelled on the interior, while the EC and fluid systems were modelled on the exterior, of a standard double-pane window. The zone details, temperature setpoints, and material properties are described in Methods).

Because the fluid multilayer, unlike the EC and RS systems, can successfully decouple infrared heat gain from visible light transmission, its thermal performance can be controlled while simultaneously optimizing for appropriate daylighting. We found that, due to this increased daylight coverage, the fluid multilayer reduced annual electric lighting energy requirements by an estimated 21% and 24% over EC and RS systems, respectively (Fig. 6f). In the winter months, due to increased solar heat gain, the fluid multilayer also saved an estimated 40% on space-heating energy compared to the EC window (Fig. 6d). This saving is substantial enough to offset the cooling energy losses in the summer months (Fig. 6e), resulting from overall efficiency tradeoffs in the optimization algorithm, to achieve an annual reduction in operational energy usage of 20% over the EC window (Fig. 6g). The RS, unable to selectively block solar heat gain while admitting daylight, suffers overheating throughout the year, consuming 112% more energy for annual space-cooling than the fluid multilayer (Fig, 6e). Solar heating limits the need for heating energy consumption, however, and the RS requires only 14% more total energy for heating, cooling, and electric lighting than the fluid multilayer overall (Fig. 6g).

Operationally, if we adjust the control algorithm to allow for spatial overlighting (>3000 lux) above 10% within the space, the fluid multilayer will increase its optical transmissivity substantially during the winter months to increase infrared-heating. Because EC windows and RSs (when down) are restricted by low solar heat gain, this change in operational control enables reductions to annual heating energy by the fluid multilayer of more than 75% and 34% over the EC and RS systems, respectively (Fig. 6d), corresponding to total energy savings of more than 43% and 36% (Fig. 6g). This energetic performance improvement suggests that the interplay between operational control and functional capacity will be crucial towards achieving truly-optimal performance.

Finally, to demonstrate feasible scalability, we estimated the energy required to operate our fluid multilayer across the year. To generate this estimate, we multiplied the energy required for a small 12 V peristaltic pump to switch a single fluidic layer within a 0.25 m^2 panel (5 W * 18 s), by the number of layers that were switched in our annual energy simulation (5100), by the number of 0.25 m^2 panels required to cover the south-face glazing (9.5 m^2) of our one-zone simulation space (38). We observe that the approximate operational energy cost of 4.8 kWh is less than 1% of the energy that our fluid multilayer can save over an EC window in simulation (873 kWh), suggesting a negligible operational energy cost that should only decrease with scale.

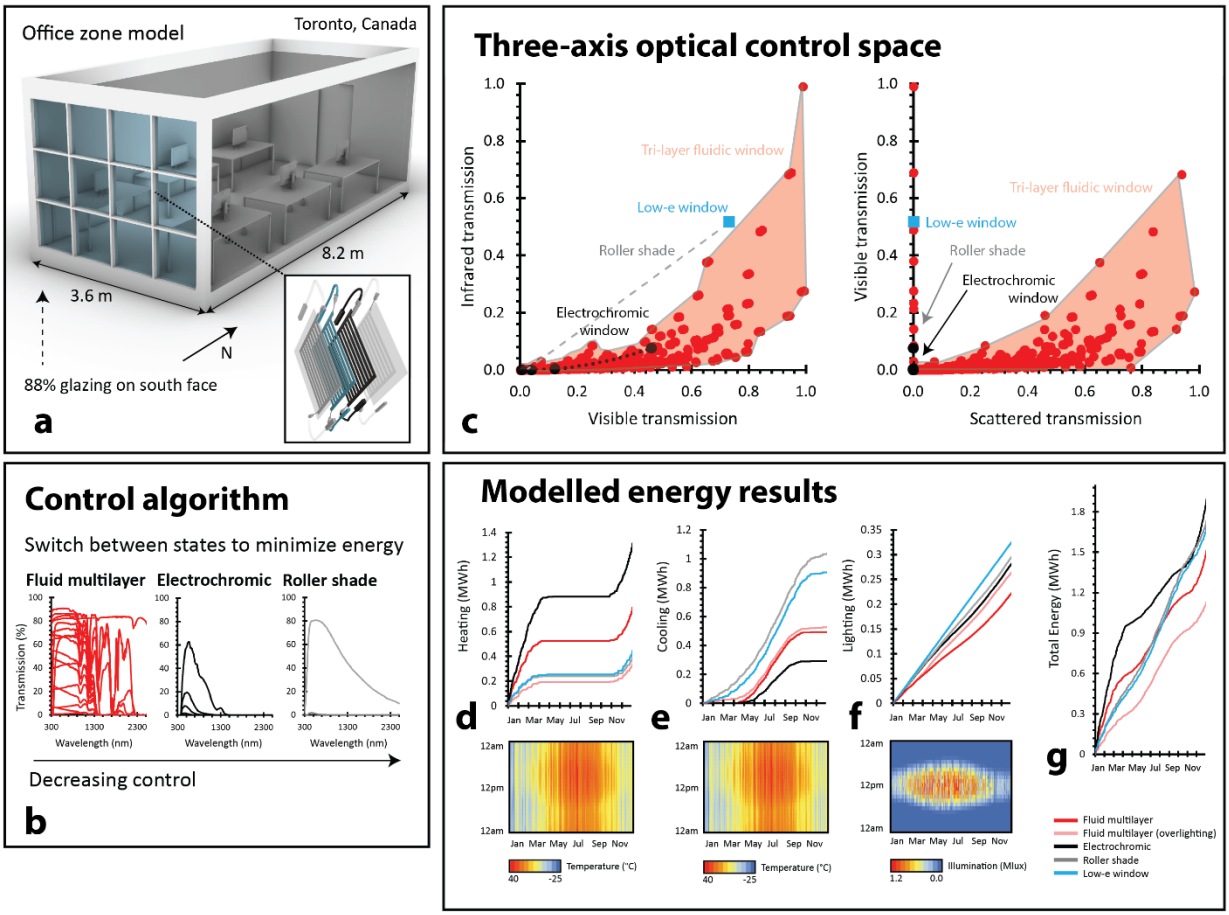

Figure 6. Fluid multilayer energy savings due to combinatorial optical tunability. (a) Reference office model for energy simulations (one-zone). Wall and roof elements are translucent only for illustrative clarity. **(b)** Demonstration of optical property range through which standard control algorithm can switch between, for fluid multilayer, EC, and RS systems. The fluid multilayer can switch between all combinations of the displayed spectral properties due to its multilayered nature. **(c)** Parameter space of all systems across visible, infrared, and scattering optical properties. A static low-e window can only address a single point in our control space. EC and RS systems can only address a curve in our control space. Our fluid multilayer can address a volume, across all three axes of our control space. Fluid multilayer (red) points represent all combinations of 16 base states from (b). **(d-f)** Simulated cumulative heating, cooling, and electric lighting energy for fluid multilayer (both with limited and unlimited spatial overlighting), EC window, RS, and low-e window across annual cycle. Data below illustrates hourly temperature and normal direct solar illumination across the year in Toronto, Canada (simulation environment). **(g)** Total simulated cumulative annual energy data for all described systems, demonstrating superior energy performance by fluid multilayer.

Discussion

We have developed a multilayer fluidic architecture for designing and tuning a building's optical response. This work demonstrates the possibility for a general fluidic mechanism, whereby small volumes of fluid can be reversibly dispersed across large surface areas to accomplish spectrally-selective absorption, transmission, and directionally-tunable scattering at scales relevant for a building. By achieving digital control over these fluid injections within multilayered devices, we were able to separate the three most important optical functions of a building facade – visible light transmission, light scattering, and infrared light transmission – towards reaching new active photo-regulatory performance, and annual energy reductions of 43% in our computational models.

Treating building functions individually might also allow us to curate a targeted local indoor environment, where, like an additive filtration system, the absorption spectra of incoming and outgoing light can be dynamically tailored through the activation of sequential liquid layers.

More broadly, this work establishes a general fluidic infrastructure for delivering customized optical responses in materials. Chemically, fluids are easily programmable and structurally, fluids are easily transportable. This unique combined performance makes fluids an underexplored 'vehicle' for carrying nanoscopic and microscopic particles that can accomplish a specific photonic function. We envision, for example, that buildings might behave as switchable greenhouses, able to admit visible and near-infrared sunlight in the day, but, through a directed switching of infrared-absorbent liquid, block long-wave infrared egress in the night. Alternatively, building surfaces with active fluid chemistries might be used to mediate human photobiology. Fluids that selectively filter specific visible wavelengths could be dispersed along the facade to achieve on-demand colour-change in response to occupant circadian dynamics, with demonstrated potential to improve human alertness, comfort, and overall health[48-50]. There also exists scope for more advanced photonic engineering, where particles can be customized to achieve various degrees of specular reflection and scattering. This broad optical programmability would allow engineers, architects, and chemists to collectively design a building's toolkit of functional responses, where custom fluid chemistries could reflect local constraints including climate, building geometry, and typology.

More practically, the ability to tune the properties of a fluid can enable climate-independent configurability. In colder climates, for instance, where glazing-integrated fluid layers might be exposed to temperatures below -20 °C, small volumes of ethanol can be added to water-based solutions to avoid the risk of freezing. This designed fluid functionality can also be coupled with strategic glazing integration. In the summer, for instance, infrared-absorbing layers are most practical on the exterior of a double pane window (this is how they were modelled in our simulations), where absorbed infrared sunlight can be conducted away to the outdoors. In the winter, however, an infrared absorbing layer might be beneficial on the interior of a double pane window, where escaping thermal energy from emissive interior bodies can instead be reradiated back indoors. We therefore speculate that our fluid layers might be integrated both on the interior or exterior of an existing glazing unit, where microelectronic components (controller and peristaltic pumps) and milli-fluid reservoirs can be housed within already-present frame constructions.

Additionally, our multilayer fluidic devices can be operated through centralized digital control (via sensors, processors, and, most critically, digitally-accessible fluid pumps). In this paper, we demonstrated a preliminary digital control algorithm, which we employed in computational simulation. Going forward, we suspect that by integrating artificial intelligence (AI) within our system's digital infrastructure, we might more effectively collect and understand real-time data, towards better predicting occupant and environmental behaviours, minimizing operational energy usage, and, ultimately, automating a building's optimal fluidic response. In the future, AI engines, via this unique digitally-driven optofluidic capability, could help buildings autonomously learn.

Finally, in practice, this active fluidic facade should help shift the opto- and thermoregulatory responsibility from mechanical systems within the building core to material systems at the building surface. Replacing reactionary systems that post-condition the indoor environment (e.g., interior air conditioners, heaters, and electric lights) with preventative systems that pre-condition the indoor environment (i.e., our multilayered system of fluid layers) can cut heating, cooling, and lighting loads nearly in half, significantly reducing the required size of mechanical systems in residences and office spaces, and the total energy needs in urban areas. The potential for this large drop in end-use power consumption may have implications for the way we design buildings, power grids, and, more broadly, the entirety of our energy infrastructure.

Materials and Methods

Device fabrication: Multilayered transparent millifluidic devices (15x15x2 cm^3) were fabricated from stacked PMMA sheets, obtained from Johnston Industrial Plastics. Channel architectures within PMMA layers were milled using a three-axis CNC-mill (AXYZ Pacer 4010 ATC). PMMA layers were adhered using the vapour-polishing

technique illustrated in Extended Data Fig. 1 and described in [47]. A needle was sealed to each channel opening using epoxy resin.

Fluid preparation and switching: Castor oil was obtained from the Heritage Store. Mineral Oil was obtained from Howard. Glycerol was obtained from BioShop (purity 99%). Carbon black particles were obtained from Davis Colors. PDMS (E200 Fluid, 10 cs) was obtained from ESCO. Silica particles were obtained from Sigma-Aldrich. Aqueous colour dyes were obtained from Club House. All aqueous suspensions and mixtures were prepared using deionized water, and were sonicated (iSonic D3200) for 120 seconds. Flow to each layer was generated with a NE-1010 digital syringe pump, or, alternatively, with a 12 V DC digital peristaltic pump (INTLLAB RS385-635). The ends of each channel (1.5 mm deep) were connected to small liquid reservoirs/syringes (14 mL) using PVC tubing (1/4" I.D., 3/8" O.D.).

Thermal imaging and optical/thermal measurements: During experimentation, PMMA surface temperature was measured with a k-type thermocouple, taped to the PMMA body. We used an incandescent light bulb as a heat source that generated a constant power of 100 W. Infrared images were taken using a FLIR E6-XT infrared camera. UV-vis-infrared spectrophotometry was performed for all fluids using a Perkin-Elmer Lambda 1050 spectrophotometer. Light intensity was measured using an Extech HD450 Light Meter Datalogger.

Simulation control algorithm: The iterative control algorithm operates as a naïve energy minimizer with conditions to maintain a set illuminance level (300 lx) in 50% of the model floor area during each occupied hour while also restricting the over-lit area (3000 lx) to less than 10% of the model floor area. During each occupied hour, 833 different control states were tested for these conditions, where each state was derived from the combination of three fluid layers that could contain 16 fluids (shown in Fig. 6b), as well as air. For each state meeting the daylight conditions, solar heat gains and electric lighting utilization were calculated. Once the acceptable daylight-driven combinations were achieved, a heat balance was conducted at each hour based upon thermal model outputs for internal gains (occupants, lights, equipment) and external gains (ventilation, solar heat gains, conduction). The state which minimized combined heating, cooling, and lighting was selected. Because thermal models are transient, where each timestep state influences the next, the control algorithm was iterated several times until annual energy results stabilized such that a near-optimal control system was achieved.

Simulation parameters: Operational energy was simulated using EnergyPlus within a standard reference office with dimensions and properties as described in [56]. Ceilings, floors, and non-exterior walls were modelled as adiabatic. The U-value of all opaque walls was defined as 0.472 W/m^{2}K. The floor was modelled with a carpet covering a 10 cm thick concrete slab. All other constructions (interior walls, exterior walls, ceiling) were steel-framed with a 1 cm thick gypsum board cover. There was 7.1 m^2 of additional exposed thermal mass from the wood furniture. The fresh air supply was modelled to be 0.0125 m^3/s/person based on occupancy. 70% of sensible, and 65% of latent heat was recovered by the heat-recovery system. Based on standard values, we set the occupancy to be 0.053821313 persons/m^2, where each person generated heat at a rate of 125 W. We set the office space to have an hourly occupancy schedule of 0, 0, 0, 0, 0, 0, 0.1, 0.2, 0.95, 0.95, 0.95, 0.95, 0.5, 0.95, 0.95, 0.95, 0.95, 0.7, 0.4, 0.4, 0.1, 0.1, 0.05, 0.05 Monday to Saturday, and an hourly occupancy schedule of 0, 0, 0, 0, 0, 0, 0.1, 0.1, 0.5, 0.5, 0.5, 0.5, 0.5, 0.5, 0.1, 0.1, 0.1, 0, 0, 0, 0, 0, 0, 0 on Sunday, where each hourly value represents a multiplier of the occupancy rate. All equipment was modelled with a peak power density of 5 W/m^2, with an hourly multiplier of 0.4, 0.4, 0.4, 0.4, 0.4, 0.4, 0.4, 0.4, 0.9, 0.9, 0.9, 0.9, 0.8, 0.9, 0.9, 0.9, 0.9, 0.8, 0.6, 0.6, 0.5, 0.5, 0.4, 0.4 from Monday to Saturday, and of 0.3 at every hour on Sunday. Temperature setpoints were defined at 21 and 24 ℃ while the building was occupied (6:00 - 22:00 on Monday-Saturday, and 6:00-18:00 on Sunday), and at 15.6 and 26.7 ℃ while the building was unoccupied. Electric lighting power across the space was 99 W, with a light power density of 3.4 W/m^2. Lights were on daily between 7:00-19:00, with dimming control activated. Dimming was regulated across three sequential room depths (2.6 m deep each) using a linear control based on the mean of all sensors within the specified depth range and a target illuminance of 500 lx. For example, if the mean luminance was 400 lx, the lighting power would be set to 20%. If the mean luminance was above 500 lx, then no lighting power would be required for that zone within the model. All interior materials were described using standard IES LM-83 values. All fluid layers were modelled on the exterior side of a low-emissivity 'control' window (SHGC = 0.71; Tvis = 0.81; U-value = 1.81 W/m2K). The simple two-state switching simulations (Fig. 5d, Extended Data Fig. 6a)

used all of the same parameters and materials, but were modelled with no occupants, electric lighting, nor equipment, and, by extension, no fresh air supply.

Extended Data

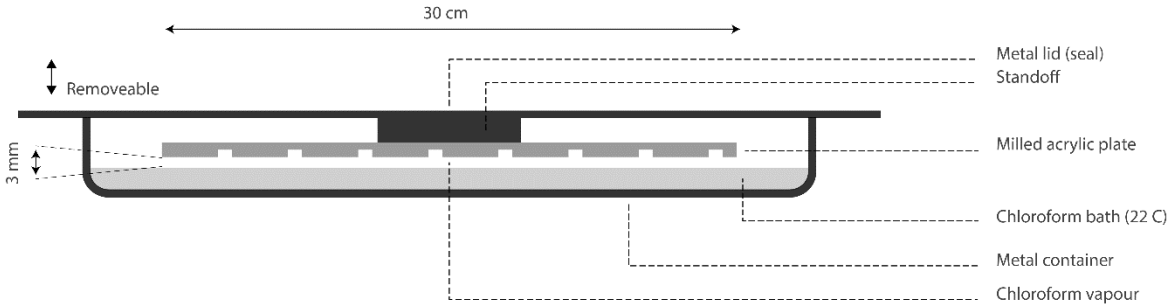

Figure 1. Diagram illustrating chloroform vapour polishing bath prior to adhering of PMMA plates. PMMA plates were exposed to bath for 3-4 minutes. Method described in more detail in [47].

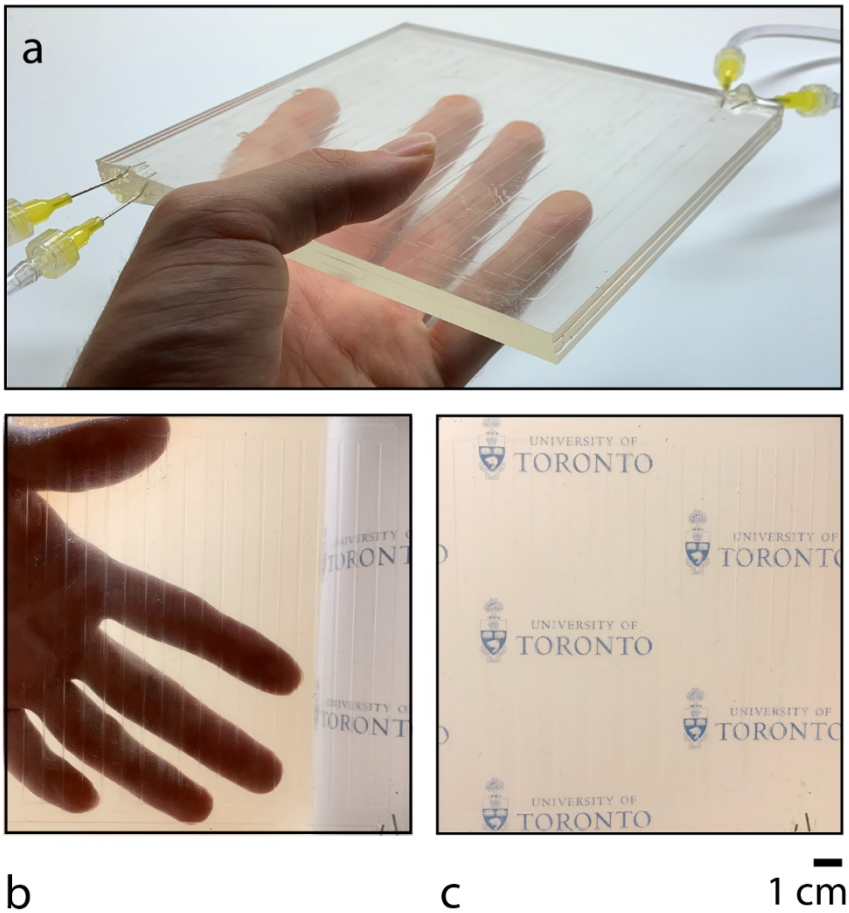

Figure 2. Photographs of bilayer device to demonstrate near-visible transparency when filled with a liquid of an equivalent refractive index to PMMA (~1.48).

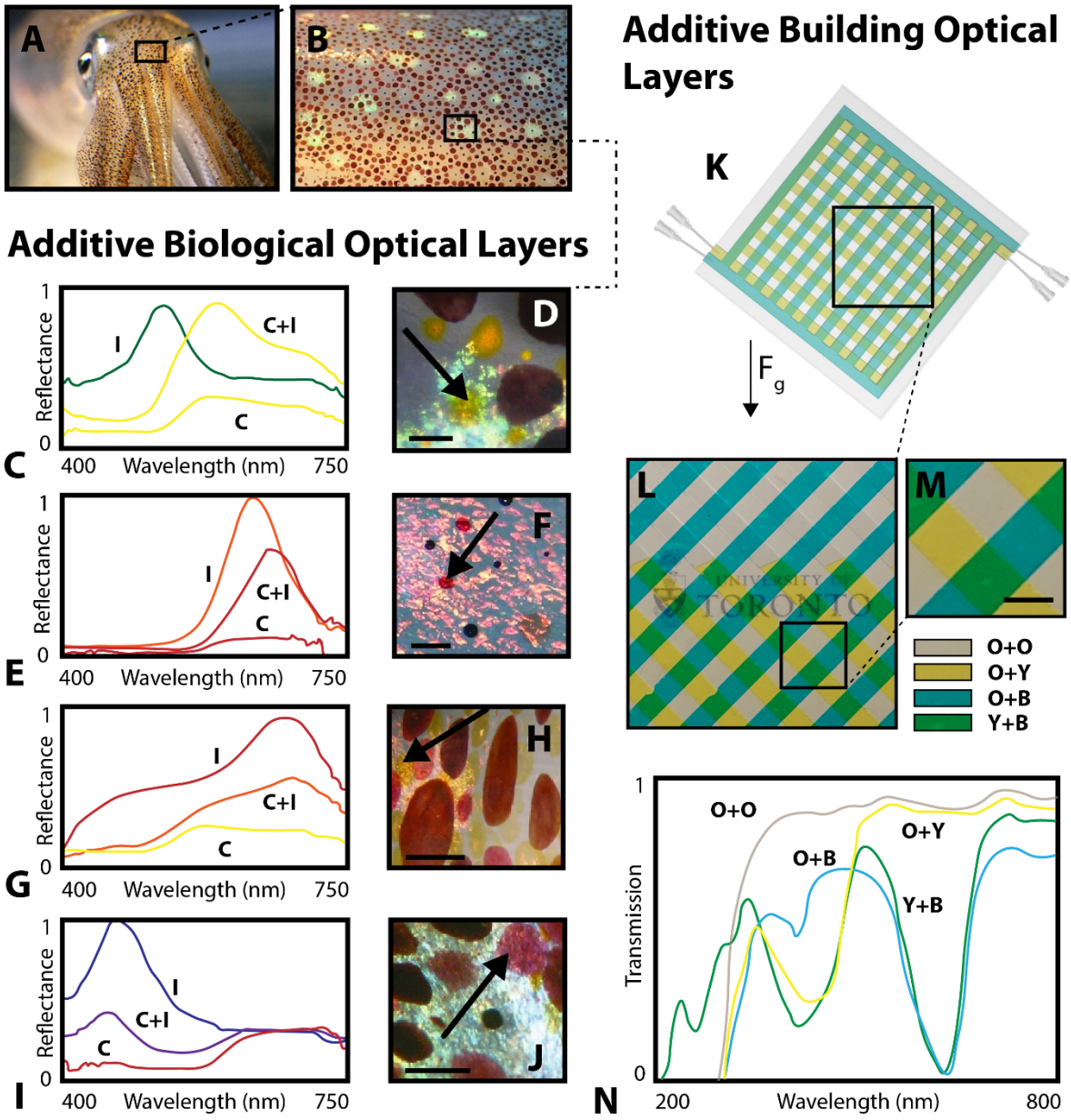

Figure 3. Comparing additive optical spectra for overlapping layers in the skin of cephalopods and for overlapping layers in our multilayered devices. (**a-b**) Skin of squid. (**c-j**) Examples of changes in optical reflectance in surface regions where chromatophores (C) and iridophores (I) overlap (C+I). (**k-n**) Analogous additive optical effects observed in bilayer fluidic devices where regions of oil (O) overlap with regions of aqueous blue dye (B) and aqueous yellow dye (Y). Image in (a) taken from [65], and image in (b) reproduced from [66], published under a Creative Commons license (http://creativecommons.org/licenses/by/4.0/). Optical spectra and images in (c-j) reproduced from [35] under license.

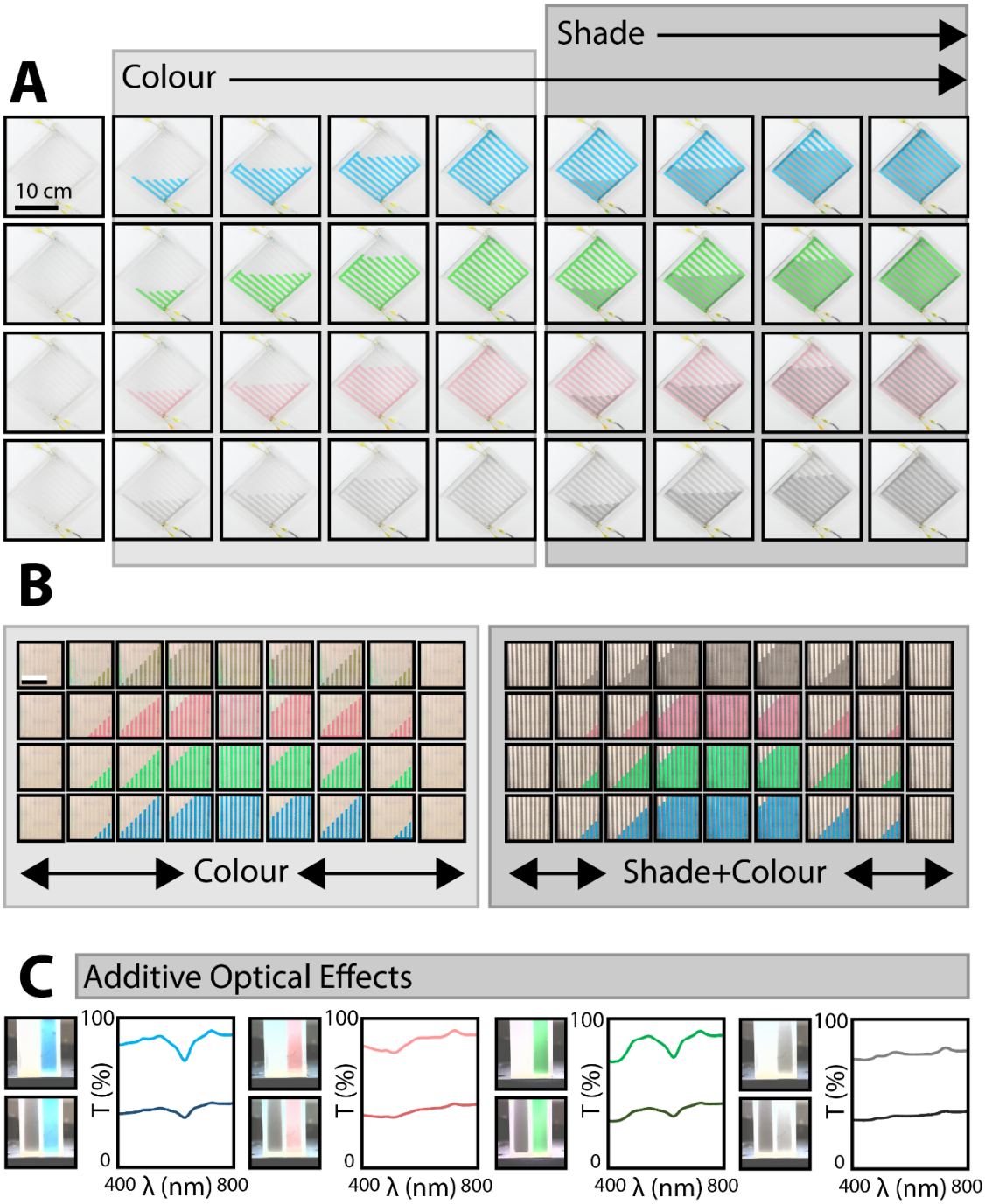

Figure 4. Additive colour change and shading in two sequential, independently-controlled, fluid layers. (**a**) Sequential injection of two fluids within bilayer device, the first an aqueous coloured dye and the second a suspension of carbon particles. Here, the effect of additive colour change and shading is demonstrated over time. (**b**) Equivalent injection of coloured fluid layers in left and right injection sequences, where back layer in left sequence is empty while back layer in right sequence is filled with shading fluid (carbon suspension). Scale bar is 10

cm. (**c**) Additive effects of multilayer fluid injection quantified across the visible region of the electromagnetic spectrum. Clear differences in transmission intensity occur when measuring bilayer cuvettes (taken to represent a model bilayer device section) in which a shading layer (left container) is activated versus left empty.

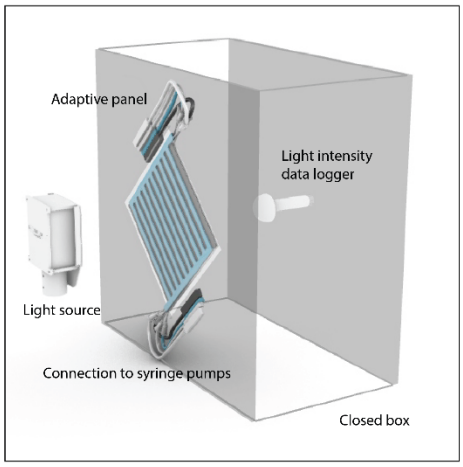

Figure 5. Physical model and experiment for measuring interior light intensity with switchable fluid injections.

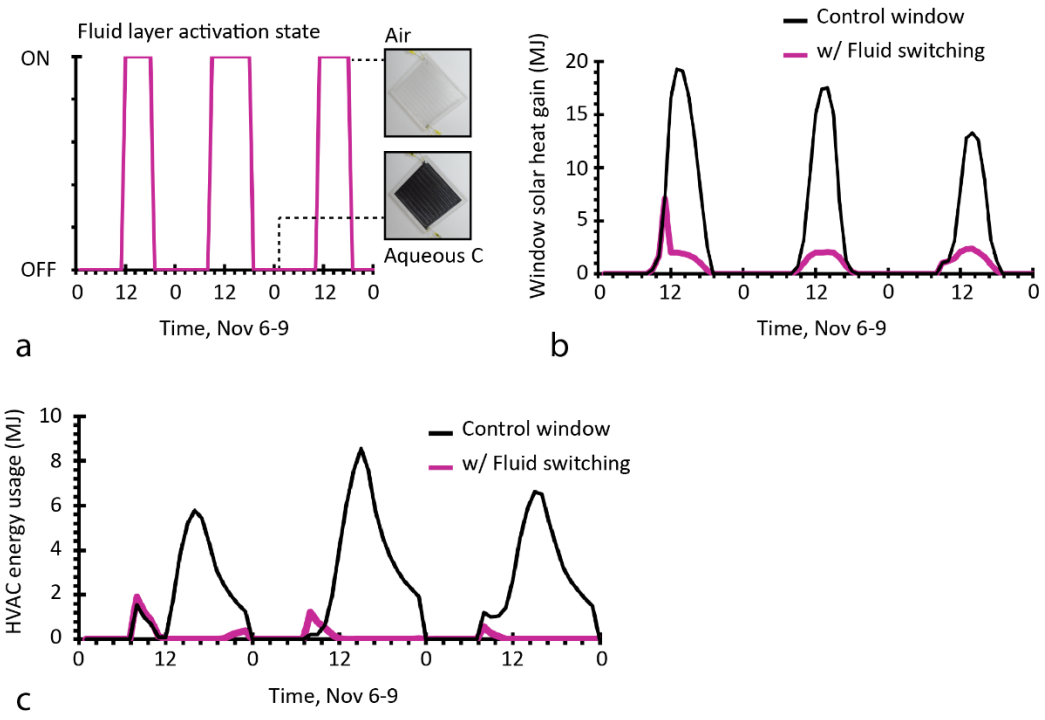

Figure 6. Simulated effect of switchable shading in buildings. Reference one-zone office for energy modelling illustrated in Fig. 6a. (**a**) Control schedule for activating light-absorbing layer within glazing. (**b**) Window solar heat gain and (**c**) associated energy usage over three-day period for both regular double-pane control window (control window) and for control window with additional switchable fluid layer. Differences in total energy predominantly reflect differences in cooling energy due to overheating.

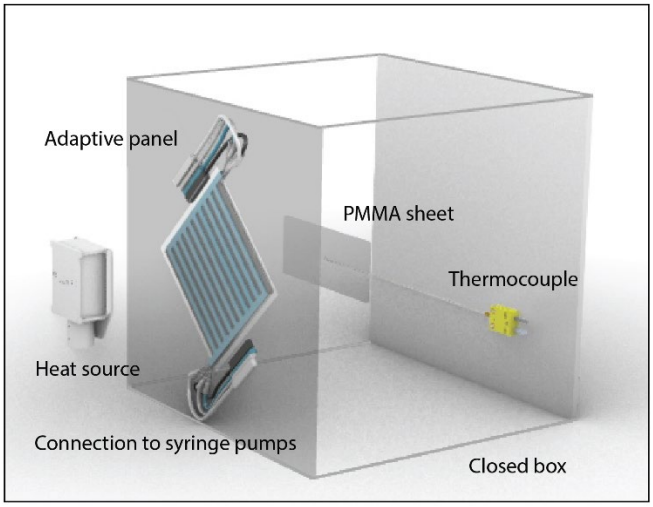

Figure 7. Physical model and experiment for measuring interior temperature with switchable fluid injections.

References

1 Loonen, R. C. G. M., Trčka, M., Cóstola, D. & Hensen, J. L. M. Climate adaptive building shells: State-of-the-art and future challenges. *Renewable and Sustainable Energy Reviews* **25**, 483-493, doi:https://doi.org/10.1016/j.rser.2013.04.016 (2013).

2 Cupelli, D., Nicoletta, F. P., Manfredi, S., Filpo, G. D. & Chidichimo, G. Electrically switchable chromogenic materials for external glazing. *Solar Energy Materials and Solar Cells* **93**, 329-333, doi:https://doi.org/10.1016/j.solmat.2008.11.010 (2009).

3 Granqvist, C. G. Electrochromics for smart windows: Oxide-based thin films and devices. *Thin Solid Films* **564**, 1-38, doi:https://doi.org/10.1016/j.tsf.2014.02.002 (2014).

4 Lee, E. S. & DiBartolomeo, D. L. Application issues for large-area electrochromic windows in commercial buildings. *Solar Energy Materials and Solar Cells* **71**, 465-491, doi:https://doi.org/10.1016/S0927-0248(01)00101-5 (2002).

5 Granqvist, C. G., Lansåker, P. C., Mlyuka, N. R., Niklasson, G. A. & Avendaño, E. Progress in chromogenics: New results for electrochromic and thermochromic materials and devices. *Solar Energy Materials and Solar Cells* **93**, 2032-2039, doi:https://doi.org/10.1016/j.solmat.2009.02.026 (2009).

6 Wang, Y., Runnerstrom, E. L. & Milliron, D. J. Switchable Materials for Smart Windows. *Annu Rev Chem Biomol Eng* **7**, 283-304, doi:10.1146/annurev-chembioeng-080615-034647 (2016).

7 Gutierrez, M. P. & Lee, L. P. Multiscale Design and Integration of Sustainable Building Functions. *Science* **341**, 247-248 (2013).

8 Stephen, E. S., Eleanor, S. L. & Øyvind, A. in *CISBAT 2003, Innovation in Building Envelopes and Environmental Systems, International Conferences on Solar Energy in Buildings.*

9 DeForest, N. *et al.* United States energy and CO2 savings potential from deployment of near-infrared electrochromic window glazings. *Building and Environment* **89**, 107-117, doi:https://doi.org/10.1016/j.buildenv.2015.02.021 (2015).

10 U.S.D.O.E. (2015).

11 IEA. (2018).

12 Messenger, J. B. Cephalopod chromatophores: neurobiology and natural history. *Biol Rev Camb Philos Soc* **76**, 473-528, doi:10.1017/s1464793101005772 (2001).
13 Mäthger, L. M., Denton, E. J., Marshall, N. J. & Hanlon, R. T. Mechanisms and behavioural functions of structural coloration in cephalopods. *Journal of The Royal Society Interface* **6**, S149-S163, doi:10.1098/rsif.2008.0366.focus (2009).
14 Khandelwal, H., Schenning, A. P. H. J. & Debije, M. G. Infrared Regulating Smart Window Based on Organic Materials. *Advanced Energy Materials* **7**, 1602209, doi:10.1002/aenm.201602209 (2017).
15 Craig, S. & Grinham, J. Breathing walls: The design of porous materials for heat exchange and decentralized ventilation. *Energy and Buildings* **149**, 246-259, doi:https://doi.org/10.1016/j.enbuild.2017.05.036 (2017).
16 Pérez-Lombard, L., Ortiz, J. & Pout, C. A review on buildings energy consumption information. *Energy and Buildings* **40**, 394-398, doi:https://doi.org/10.1016/j.enbuild.2007.03.007 (2008).
17 Pan, C.-A. & Jeng, T. Cellular Robotic Architecture. *International Journal of Architectural Computing* **10**, 319-339, doi:10.1260/1478-0771.10.3.319 (2012).
18 Attia, S. Evaluation of adaptive facades: The case study of Al Bahr Towers in the UAE. *QScience Connect* **2017**, doi:https://doi.org/10.5339/connect.2017.qgbc.6 (2018).
19 Lienhard, J. *et al.* Flectofin: a hingeless flapping mechanism inspired by nature. *Bioinspiration & Biomimetics* **6**, 045001, doi:10.1088/1748-3182/6/4/045001 (2011).
20 Drozdowski, Z. & Gupta, S. in *Proceedings of the 29th Annual Conference of the Association for Computer Aided Design in Architecture.* 105-109.
21 Park, D. *et al.* Dynamic daylight control system implementing thin cast arrays of polydimethylsiloxane-based millimeter-scale transparent louvers. *Building and Environment* **82**, 87-96, doi:https://doi.org/10.1016/j.buildenv.2014.07.016 (2014).
22 Ge, D. *et al.* A Robust Smart Window: Reversibly Switching from High Transparency to Angle-Independent Structural Color Display. *Advanced Materials* **27**, 2489-2495, doi:https://doi.org/10.1002/adma.201500281 (2015).
23 DeForest, N., Shehabi, A., Selkowitz, S. & Milliron, D. J. A comparative energy analysis of three electrochromic glazing technologies in commercial and residential buildings. *Applied Energy* **192**, 95-109, doi:https://doi.org/10.1016/j.apenergy.2017.02.007 (2017).
24 Cupelli, D. *et al.* Self-adjusting smart windows based on polymer-dispersed liquid crystals. *Solar Energy Materials and Solar Cells* **93**, 2008-2012, doi:https://doi.org/10.1016/j.solmat.2009.08.002 (2009).
25 Drzaic, P. S. Polymer dispersed nematic liquid crystal for large area displays and light valves. *Journal of Applied Physics* **60**, 2142-2148, doi:10.1063/1.337167 (1986).
26 Van Konynenburg, P., Marsland, S. & McCoy, J. Solar radiation control using NCAP liquid crystal technology. *Solar Energy Materials* **19**, 27-41, doi:https://doi.org/10.1016/0165-1633(89)90021-X (1989).
27 Ghosh, A., Norton, B. & Duffy, A. Daylighting performance and glare calculation of a suspended particle device switchable glazing. *Solar Energy* **132**, 114-128, doi:https://doi.org/10.1016/j.solener.2016.02.051 (2016).
28 Lampert, C. M. Chromogenic smart materials. *Materials Today* **7**, 28-35, doi:https://doi.org/10.1016/S1369-7021(04)00123-3 (2004).
29 Granqvist, C. G. Transparent conductors as solar energy materials: A panoramic review. *Solar Energy Materials and Solar Cells* **91**, 1529-1598, doi:https://doi.org/10.1016/j.solmat.2007.04.031 (2007).

30 Granqvist, C. G. Chromogenic materials for transmittance control of large-area windows. *Critical Reviews in Solid State and Materials Sciences* **16**, 291-308, doi:10.1080/10408439008242184 (1990).
31 Wood, D. M., Correa, D., Krieg, O. D. & Menges, A. Material computation—4D timber construction: Towards building-scale hygroscopic actuated, self-constructing timber surfaces. *International Journal of Architectural Computing* **14**, 49-62, doi:10.1177/1478077115625522 (2016).
32 Reichert, S., Menges, A. & Correa, D. Meteorosensitive architecture: Biomimetic building skins based on materially embedded and hygroscopically enabled responsiveness. *Computer-Aided Design* **60**, 50-69, doi:https://doi.org/10.1016/j.cad.2014.02.010 (2015).
33 Li, X.-H., Liu, C., Feng, S.-P. & Fang, N. X. Broadband Light Management with Thermochromic Hydrogel Microparticles for Smart Windows. *Joule* **3**, 290-302, doi:https://doi.org/10.1016/j.joule.2018.10.019 (2019).
34 Yu, C. *et al.* Adaptive optoelectronic camouflage systems with designs inspired by cephalopod skins. *Proc Natl Acad Sci U S A* **111**, 12998-13003, doi:10.1073/pnas.1410494111 (2014).
35 Mäthger, L. M. & Hanlon, R. T. Malleable skin coloration in cephalopods: selective reflectance, transmission and absorbance of light by chromatophores and iridophores. *Cell and Tissue Research* **329**, 179, doi:10.1007/s00441-007-0384-8 (2007).
36 Sutherland, R. L., Mäthger, L. M., Hanlon, R. T., Urbas, A. M. & Stone, M. O. Cephalopod coloration model. II. Multiple layer skin effects. *J Opt Soc Am A Opt Image Sci Vis* **25**, 2044-2054, doi:10.1364/josaa.25.002044 (2008).
37 Hanlon, R. T. *et al.* Cephalopod dynamic camouflage: bridging the continuum between background matching and disruptive coloration. *Philos Trans R Soc Lond B Biol Sci* **364**, 429-437, doi:10.1098/rstb.2008.0270 (2009).
38 Deravi, L. F. *et al.* The structure-function relationships of a natural nanoscale photonic device in cuttlefish chromatophores. *J R Soc Interface* **11**, 20130942-20130942, doi:10.1098/rsif.2013.0942 (2014).
39 Wardill, T. J., Gonzalez-Bellido, P. T., Crook, R. J. & Hanlon, R. T. Neural control of tuneable skin iridescence in squid. *Proc Biol Sci* **279**, 4243-4252, doi:10.1098/rspb.2012.1374 (2012).
40 Morse, D. E. & Taxon, E. Reflectin needs its intensity amplifier: Realizing the potential of tunable structural biophotonics. *Applied Physics Letters* **117**, 220501, doi:10.1063/5.0026546 (2020).
41 Teyssier, J., Saenko, S. V., van der Marel, D. & Milinkovitch, M. C. Photonic crystals cause active colour change in chameleons. *Nature Communications* **6**, 6368, doi:10.1038/ncomms7368 (2015).
42 Phillips, P. K. & Heath, J. E. Heat exchange by the pinna of the African elephant (Loxodonta africana). *Comp Biochem Physiol Comp Physiol* **101**, 693-699, doi:10.1016/0300-9629(92)90345-q (1992).
43 Tattersall, G. J., Andrade, D. V. & Abe, A. S. Heat Exchange from the Toucan Bill Reveals a Controllable Vascular Thermal Radiator. *Science* **325**, 468, doi:10.1126/science.1175553 (2009).
44 Hatton, B. D. *et al.* An artificial vasculature for adaptive thermal control of windows. *Solar Energy Materials and Solar Cells* **117**, 429-436, doi:https://doi.org/10.1016/j.solmat.2013.06.027 (2013).
45 Auerswald, L., Freier, U., Lopata, A. & Meyer, B. Physiological and morphological colour change in Antarctic krill, Euphausia superba: a field study in the Lazarev Sea. *Journal of Experimental Biology* **211**, 3850, doi:10.1242/jeb.024232 (2008).
46 Rassart, M., Colomer, J. F., Tabarrant, T. & Vigneron, J. P. Diffractive hygrochromic effect in the cuticle of the hercules beetle Dynastes hercules. *New Journal of Physics* **10**, 033014, doi:10.1088/1367-2630/10/3/033014 (2008).

47 Ogilvie, I. R. G. *et al.*
48 Cajochen, C., Zeitzer, J. M., Czeisler, C. A. & Dijk, D. J. Dose-response relationship for light intensity and ocular and electroencephalographic correlates of human alertness. *Behav Brain Res* **115**, 75-83, doi:10.1016/s0166-4328(00)00236-9 (2000).
49 Gooley, J. J. *et al.* Exposure to room light before bedtime suppresses melatonin onset and shortens melatonin duration in humans. *J Clin Endocrinol Metab* **96**, E463-E472, doi:10.1210/jc.2010-2098 (2011).
50 Abeysuriya, R. G., Lockley, S. W., Robinson, P. A. & Postnova, S. A unified model of melatonin, 6-sulfatoxymelatonin, and sleep dynamics. *J Pineal Res* **64**, e12474, doi:10.1111/jpi.12474 (2018).
51 Corner, T. C. (YouTube, 2019).
52 Papaefthimiou, S., Syrrakou, E. & Yianoulis, P. Energy performance assessment of an electrochromic window. *Thin Solid Films* **502**, 257-264, doi:https://doi.org/10.1016/j.tsf.2005.07.294 (2006).
53 Kay, R., Nitiema, K., Katrycz, C., Jakubiec, A. & Hatton, B. D. Self-organizing fluids for active building facades (under review). (2021).
54 Swinehart, D. F. The beer-lambert law. *Journal of chemical education* **39**, 333 (1962).
55 Ward, G. J. in *Proceedings of the 21st annual conference on Computer graphics and interactive techniques* 459–472 (Association for Computing Machinery, 1994).
56 Reinhart, C. F., Jakubiec, J. A. & Ibarra, D.
57 Ceylan, H. & Myers, G. E. Long-Time Solutions to Heat-Conduction Transients with Time-Dependent Inputs. *Journal of Heat Transfer-transactions of The Asme* **102**, 115-120 (1980).
58 Energy, U. S. D. o. EnergyPlus Version 9.5.0 Engineering Reference. (2021).
59 Boubekri, M., Cheung Ivy, N., Reid Kathryn, J., Wang, C.-H. & Zee Phyllis, C. Impact of Windows and Daylight Exposure on Overall Health and Sleep Quality of Office Workers: A Case-Control Pilot Study. *Journal of Clinical Sleep Medicine* **10**, 603-611, doi:10.5664/jcsm.3780 (2014).
60 Hopkinson, R. G. Glare from daylighting in buildings. *Appl Ergon* **3**, 206-215, doi:10.1016/0003-6870(72)90102-0 (1972).
61 Jakubiec, J. *Validation of Simplified Visual Discomfort Calculations*. (2018).
62 Karlsson, J. & Roos, A. Annual energy window performance vs. glazing thermal emittance — the relevance of very low emittance values. *Thin Solid Films* **392**, 345-348, doi:https://doi.org/10.1016/S0040-6090(01)01055-0 (2001).
63 Martín-Palma, R. J. Spectrally selective coatings on glass: solar-control and low-emissivity coatings. *Journal of Nanophotonics* **3**, 030305 (2009).
64 Ye, H., Meng, X., Long, L. & Xu, B. The route to a perfect window. *Renewable Energy* **55**, 448-455, doi:https://doi.org/10.1016/j.renene.2013.01.003 (2013).
65 Look, D. (YouTube, 2015).
66 Williams, T. L. *et al.* Dynamic pigmentary and structural coloration within cephalopod chromatophore organs. *Nature Communications* **10**, 1004, doi:10.1038/s41467-019-08891-x (2019).

Acknowledgments

We acknowledge the help of Nicholas Hoban and Paul Kozak for providing device fabrication assistance. And we thank Mathias Kolle for providing invaluable advice on optical experimentation techniques.

Funding

Canadian Foundation for Innovation (CFI) #31799 (BDH)
Percy Edward Hart Professorship, University of Toronto (BDH)

RK was supported by a Canada Graduate Scholarship, a C.W. Bowman Graduate Scholarship, and a Bert Wasmund Graduate Fellowship.

Author contributions
Conceptualization: RK, BDH
Methodology: RK, CK, BDH
Physical experimentation: RK
Simulation and control algorithm design: JAJ
Funding acquisition: BDH
Writing – first draft: RK
Writing – final draft: RK, JAJ, CK, BDH

Additional Information
Supplementary Information is available for this paper.
Correspondence and requests for materials should be addressed to raphael.kay@mail.utoronto.ca,

Competing interests: Authors declare that they have no competing interests.
Data and materials availability: All data will be made available by the authors upon request.